Usage guidelines

Multi scale modelling of hybrid glass fibres reinforced graphene platelets polyamide PA6 matrix composites for crashworthiness applications

Ahmed Elmarakbi[1*], Wiyao Azoti[1] and Mohamed Serry[2]

[1]*Automotive Composites Group, Faculty of Engineering and Advanced and Manufacturing, University of Sunderland, Sunderland, SR6 0DD, UK*

[2]*Department of Mechanical Engineering, The American University in Cairo, Cairo, Egypt*

[*]Email: ahmed.elmarakbi@sunderland.ac.uk, Tel:+441915153877

Abstract: This work investigates the crashworthiness response for a hierarchical modelling of hybrid composite material consisting of short-glass fibres reinforced graphene platelets polyamide PA6 matrix. A multi scale approach, using both mean-field homogenisation and finite element FE techniques, is employed to derive the overall response. Graphene is considered as platelets GPL embedded within an elasto plastic matrix phase. The 2-phases composite response is therefore computed under the Mori-Tanaka micromechanics scheme by accounting for the GPL spatial orientation. The modelling of the 3-phases short glass fibres/graphene polymer composite consists on a double-scale approach combining the 2-phases graphene polymer composite as matrix phase in which are embedded the glass fibres. Numerical characterisations involving tensile, compression, fracture toughness and Charpy impact tests enable the determination of damage/failure thresholds for crashworthiness applications. The full crash box is simulated by implementing the constitutive 3-phases composite using a user-defined Digimat/LS-DYNA linkage. Numerical results, which are compared to those from conventional steel and glass fibres composites, show the contribution of the GPL volume fraction in the improvement of the specific energy absorption SEA.

Keywords: Graphene platelets, Polymer composites, Multiscale simulation, Numerical characterisation, Crashworthiness.

1. Introduction

Passenger safety represents a major design parameter on which legislation remains continuously tough. Whilst, the global trend in automotive engineering is oriented toward lightweight materials for energy efficiency, safety issues are as well of a particular interest. Therefore, new materials with high energy absorption capabilities need to be developed to overcome the well-known lightweighting-safety trade-off. For such a purpose, composite materials for instance fibres reinforced plastics have been developed with an attractive benefit of a great capability of weight reduction with high energy absorption levels during crash situations [1, 2]. Therefore, the use of composite materials in structures as energy absorbers is rapidly growing because composites exhibit a significantly higher energy absorption capacity per unit weight than metals [3, 4]. Since, the effective response of the composite depends on the design of its microstructure, intensive investigations are continuously being led in the direction of new composite fillers. Recently, the discovery of the graphene has opened new windows for the design of multifunctional materials.

Graphene is at the centre of a growing academic and industrial interest because it can produce a dramatic improvement in mechanical properties at low filler content [5]. Indeed, it is expected that one of the most immediate application for graphene will be in composite materials [6]. To take a full advantage of its properties, integration of individual graphene sheets in polymer matrices is important. Exceptional physical and mechanical properties, a high surface/volume ratio and low filler content of graphene make the graphene a promising candidate for developing the next-generation of high performance polymer composites [5, 7-13]. Theoretical and numerical studies involving graphene related materials have been developed based on the combination of atomistic simulations and continuum and structural mechanics. Micromechanics based analytical derivations from molecular interatomic potentials (modified-Morse, Lennard-Jones potentials) [14, 15] as well as FE simulations [16-20] have been developed to derive the overall properties of the graphene nanocomposites. While the combination of atomistic and continuum approaches could be considered as the most powerful computational tool to address the problems associated with different scales, these models require especially high computational costs as reported by Dai et al. [21]. As a common assumption in most of numerical studies, the graphene is modelled as platelets with a diameter to thickness ratio of a disc commonly called aspect ratio AR [22].

The goal of this work is to analyse the response of an automotive crash box composite consisting on a hybrid short glass fibres reinforced graphene platelets polymer matrix composites. In order to assess the contribution of the graphene, a hierarchical modelling framework based on analytical as well as finite element techniques is employed to derive the overall composite response and subsequently the mechanical characterisation for the macroscopic crashworthiness. Graphene sheets are considered as platelets GPL embedded within an elasto plastic polyamide PA6 matrix phase leading to a 2-phases graphene/polymer composite. The modelling of the 3-phases short glass fibres/graphene polymer composite consists on a double-scale approach combining the 2-phases graphene polymer composite as matrix phase in which are embedded the glass fibres. The full structure crash box is simulated at each Gauss integration point by implementing the constitutive 3-phases composite using a user-defined materials subroutine.

The paper is organised as follows: section 2 establishes the theoretical framework for deriving the effective properties of a composite and recalls the procedure for obtaining the nonlinear tangent operators. The modelling of the 2-phases composite is presented in section 3 along with the numerical characterisation of the 3-phases composite and the full structure simulation. Numerical results obtained for the crashworthiness application are presented in section 4.

2. Theoretical background

2.1. General considerations

A macroscopic homogeneous and microscopic heterogeneous materials is selected under a representative volume element RVE. The associated boundary-value problems are formulated, in the terms of uniform macro field traction vector or linear displacement fields. The RVE is assumed in equilibrium and its overall deformation compatible. Also the body forces and inertia term are neglected. The effective properties are given by:

$$C_{ijkl}^{eff} = \frac{1}{V} \int_V c_{ijmn}(r) A_{mnkl}(r) dV \qquad (1)$$

Or in others terms

$$C^{eff} = c^0 + \sum_{I=1}^{N} f_I \left(c^I - c^0 \right) : A^I \qquad (2)$$

with c^I, A^I, f_I the uniform stiffness tensor, the global strain concentration tensor and the volume fraction of phase I, respectively. The global strain concentration tensor A represents the unknown parameter which contains all information about the microstructure. Its expression is given by an iterative procedure [23] such as:

$$\begin{cases} A^I = a^I : \left\langle a^I \right\rangle^{-1} \\ \left(a^I \right)_0 = I \\ \left(a^I \right)_{i+1} = \left(I + T^{II} : \Delta c^I \right)^{-1} : \left(I - \sum_{\substack{J=0 \\ J \neq I}}^{N} T^{IJ} : \Delta c^J : \left(a^J \right)_i \right) \\ I = 0,1,2,3,\ldots\ldots, N \end{cases} \qquad (3)$$

with $\Delta c^J = c^J - C^r$ and C^r is defined as uniform stiffness tensor of a homogeneous reference medium. a^I stands for the local strain concentration tensor and T^{IJ} represents the interaction tensor between inclusions within the RVE. It is expressed such as:

$$T^{IJ} = \frac{1}{V^I} \int_{V^I} \int_{V^J} \Gamma(r - r') dV dV' \qquad (4)$$

with $\Gamma(r - r')$ being the modified Green tensor. When the Mori-Tanaka scheme is selected, the reference medium is assumed to be the matrix phase leading to $C^R = c^0$. Also, the average strain field inside the matrix is approximated by the strain within the reference medium leading to $a^0 = I$. Based on these assumptions, the effective Mori-Tanaka properties are given by:

$$C^{MT} = \sum_{I=0}^{N} f_I c^I A^I = \left(f_0 c^0 + \sum_{I=1}^{N} f_I c^I a^I \right) : A^0 \qquad (5)$$

with A^0 denoting the global strain concentration tensor of the matrix. Its expression yields:

$$A^0 = a^0 : \left\langle a^I \right\rangle^{-1} = \left(f_0 I + \sum_{I=1}^{N} f_I a^I \right)^{-1} \qquad (6)$$

▪ **Case of two (2)-phases composite materials**

In the case of one-site version of the above equations, the interactions between inclusion I and its neighbours J are neglected, i.e. all the $T^{IJ} = 0$. The local strain concentration tensor a^I becomes more simply:

$$a^I = \left[I + T^{II} : \Delta c^I \right]^{-1} = \left[I + S : \left(C^r \right)^{-1} : \Delta c^I \right]^{-1} \qquad (7)$$

3

where $\mathbf{S}$ denotes the Eshelby's tensor and $C^r = c^0$ in the present case of Mori-Tanaka scheme. The global strain concentration tensor within the matrix is given by:

$$A^0 = \left[f_I a^I + \left(1 - f_I \right) \mathbf{I} \right]^{-1} \tag{8}$$

Substituting equation (8) in equation (5) for the case of 2-phases composite, the effective properties yields:

$$C^{MT} = \left[\left(1 - f_I \right) c^0 + f_I c^I : a^I \right] : \left[f_I a^I + \left(1 - f_I \right) \mathbf{I} \right]^{-1} \tag{9}$$

2.2. Elasto-plastic Tangent Operators

Within the RVE, let us assume that one or more phases behave elasto-plastically. Referring to the work by Doghri and Ouaar [24] at least two tangent operators can be defined: the "continuum" (or elasto-plastic) C^{ep} tangent operator, which is derived from the rate constitutive equation, and the "consistent" (or algorithmic) C^{alg} tangent operator, which is solved by a discretisation in the time interval $\left[t_n, t_{n+1} \right]$. These tangent operators are related to the rate of the constitutive equation as follows:

$$\begin{cases} \dot{\boldsymbol{\sigma}} = C^{ep} : \dot{\boldsymbol{\varepsilon}} \\ \delta \boldsymbol{\sigma}_{n+1} = C^{alg} : \delta \boldsymbol{\varepsilon}_{n+1} \end{cases} \tag{10}$$

They are derived from the classical J_2 flow rule:

$$\begin{cases} \boldsymbol{\sigma} = C^{el} : \left(\boldsymbol{\varepsilon} - \boldsymbol{\varepsilon}^p \right) \\ f = \sigma_{eq} - R(p) - \sigma_Y \\ \dot{\boldsymbol{\varepsilon}}^p = \dot{p} N, \quad N = \dfrac{\partial f}{\partial \boldsymbol{\sigma}} = \dfrac{3}{2} \dfrac{dev(\boldsymbol{\sigma})}{\sigma_{eq}} \\ \sigma_{eq} = \left(\dfrac{3}{2} s : s \right)^{1/2} \end{cases} \tag{11}$$

The "continuum" (or elasto-plastic) C^{ep} tangent operator yields:

$$\begin{cases} C^{ep} = C^{el} - \dfrac{\left(2\mu \right)^2}{h} N \otimes N \\ h = 3\mu + \dfrac{dR}{dp} > 0 \end{cases} \tag{12}$$

while the "consistent" (or algorithmic) C^{alg} tangent operator is given by:

4

$$\begin{cases} \boldsymbol{C}^{a\lg} = \boldsymbol{C}^{ep} - \left(2\mu\right)^2 \Delta p \dfrac{\sigma_{eq}}{\sigma_{eq}^{tr}} \dfrac{\partial \boldsymbol{N}}{\partial \boldsymbol{\sigma}} \\[2ex] \dfrac{\partial \boldsymbol{N}}{\partial \boldsymbol{\sigma}} = \dfrac{1}{\sigma_{eq}} \dfrac{3}{2} \mathbf{I}^{dev} - \boldsymbol{N} \otimes \boldsymbol{N} \end{cases} \tag{13}$$

In equations (12) and (13), μ denotes the material shear modulus while $\boldsymbol{C}^{el}$ represents the elastic stiffness tensor and $R(p)$ is the hardening stress function with p the accumulated plastic strain. $\boldsymbol{N}$ represents the normal to the yield surface in the stress space. σ_{eq}^{tr} denotes a trial elastic predictor of σ_{eq}, $\mathbf{I}^{dev}$ stands for the deviatoric part of the fourth order symmetric identity tensor.

3. Hierarchical modelling of the hybrid composite

3.1. Modelling of the two (2)-phases composite

The modelling strategy for the 2-phases composite consists by reinforcing the polymer matrix by graphene platelets. The GPL are modelled under DIGIMAT-MF [25] tools. This strategy is shown by Figure 1 where a RVE describing two spatial distributions (aligned 2D versus random 3D configurations) is studied. The matrix is an elasto-plastic polyamide PA6-B3K with an isotropic hardening in power-law whereas the GPL are considered elastic. The properties of the matrix and the GPL are reported in Table1 and Table 2, respectively.
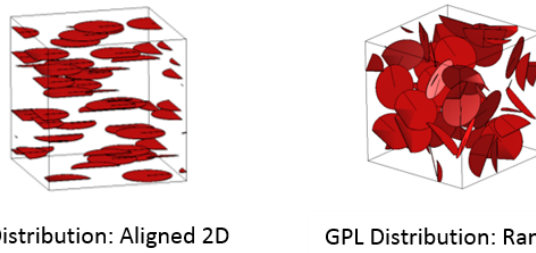
Table 1. Material properties of graphene platelets

Phase	Graphene G2NAN
Density	2.2 mg/cm^3
Poisson's ratio	0.22
Young's Modulus	1000 GPa
Tensile Strength	5 GPa
Thickness	10 nm
Ave lateral size	30 micron
Aspect Ratio	0.000333

Table 2. Material properties of the polyamide PA6 matrix

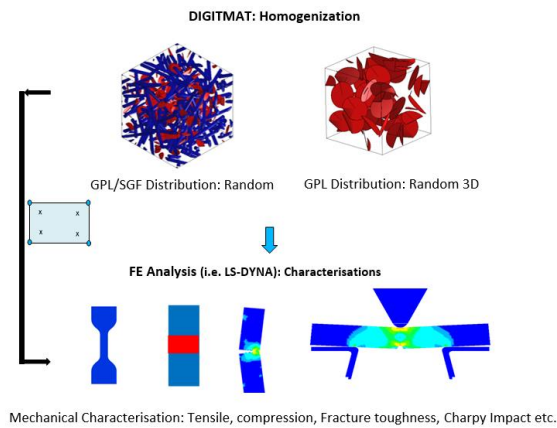| Phase	PA6-B3K
Density	1.13 mg/cm^3
Poisson's ratio	0.39
Young's Modulus	2000 MPa
Yield Stress	60.5 MPa
Hardening Modulus	63 MPa
Hardening Model	Power law
Hardening exponent	0.4

Figure 1. 2-phases composite modelling for GPL distribution

3.2. Modelling of the three (3)-phases composite

The modelling of 3-phases short glass fibres/graphene polyamide composite is based on a double-scale approach combining the 2-phases graphene polyamide composite used as matrix in which are embedded the short glass fibres. Material properties of the short glass fibres are gathered in Table 3. The derivation of the effective properties remains analytical-based micromechanics formalism. Mechanical characterisations based on the ASTM standards are performed on tensile [26], compression [27], fracture toughness [28] as well as Charpy impact [29] specimens (Figure 2). Their results enable the determination of the damage/failure thresholds for crashworthiness applications.

Table 3. Material properties of the short glass fibres

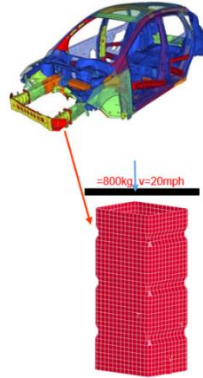| Phase	S-Glass Fibres
Density	2.49 mg/cm^3
Poisson's ratio	0.22
Young's Modulus	89 GPa
Tensile Strength	4750 MPa
Compressive Strength	4500 MPa
Aspect Ratio	23.5

Figure 2. 3-phases composite modelling and a FE characterisation

3.3. Macroscale FE simulation of a crash box

The crashworthiness is simulated for the 3-phases composite. A multiscale strategy embedding developments at the previous sections are linked at each integration point of a crash box.
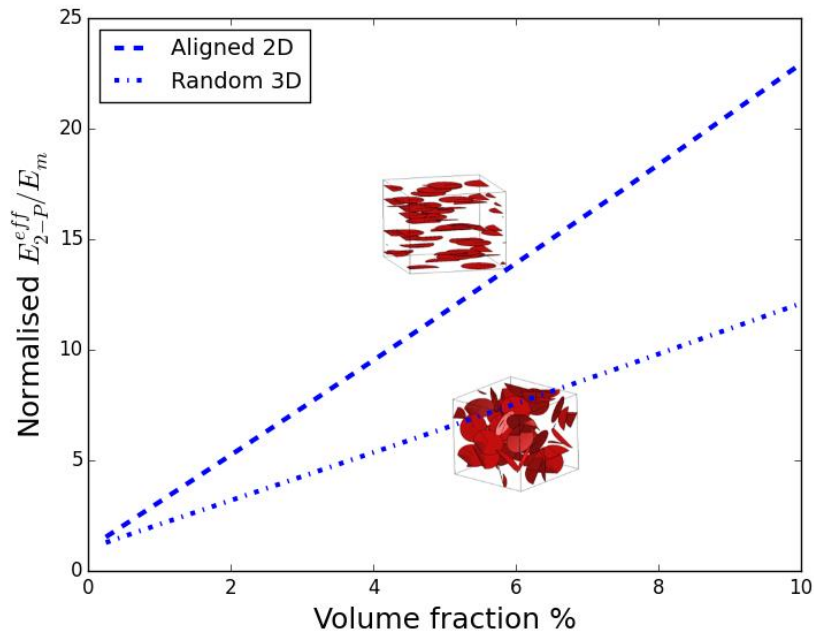

Figure 3. Numerical model of the crash box

The geometry of the crash box depicted by Figure 3 is created under LS-DYNA FE software [30]. Shell elements S4R are used for meshing purposes. The crushing load is applied on one side (upper) of the box through a rigid plate moving at a constant velocity (20mph). The other (lower) side of the box is fully constrained. Contact capabilities in LS-DYNA /EXPLICIT mainly *CONTACT_AUTOMATIC_SINGLE_SURFACE are used to define the contact interactions between different parts of the model. The constitutive mechanical law implemented in the crash box results from a user subroutine *MAT_USER_DEFINED_MATERIAL_MODELS. The linkage DIGIMAT-CAE/LS-DYNA [25] is employed for passing the microscale data resulting from the 3-phases composite modelling to the full macroscale representing the crash box. In addition, the simulation requires inputs of damage initiation and evolution resulting from the above sections. Failed continuum shell elements are removed using a damage-based element deletion.
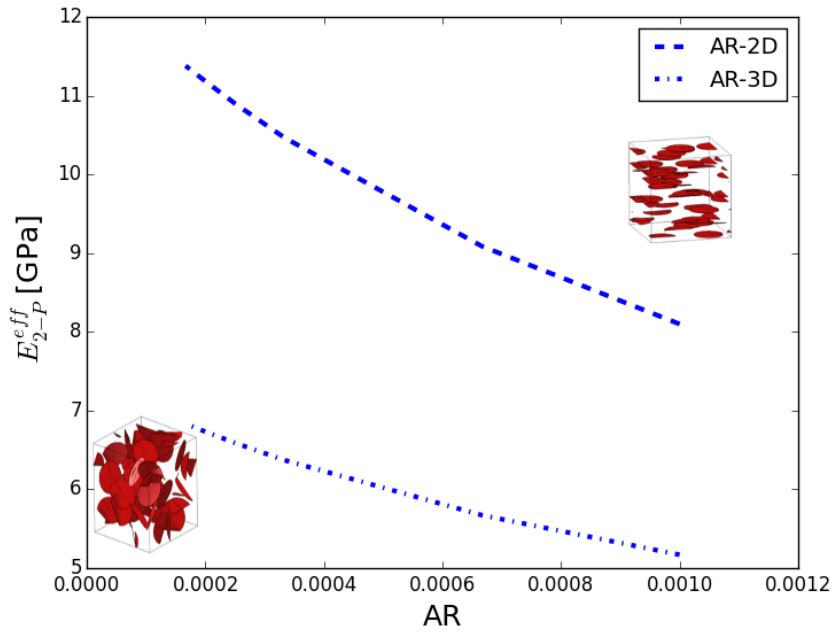
4. Numerical results and discussions

4.1. Two (2)-phases composite

A RVE describing two spatial distributions (aligned 2D versus random 3D) of GPL are considered for numerical applications. Figure 4 depicts the evolution of the normalised effective Young modulus E_{2-P}^{eff}/E_m versus the GPL volume fraction. The results indicate an increase of E_{2-P}^{eff}/E_m with the GPL volume fraction evolution. In addition, the aligned 2D distribution shows more effective improvement compared to the random 3D. Furthermore, the evolution of E_{2-P}^{eff} versus the GPL aspect ratio AR is analysed for both distributions. Indeed, results in Figure 5 show a decrease of E_{2-P}^{eff} when the AR increases. The higher the AR, the lower the effective Young modulus E_{2-P}^{eff}. The aligned 2D distribution shows more effective reinforcement behaviour with respect to the random 3D distribution.
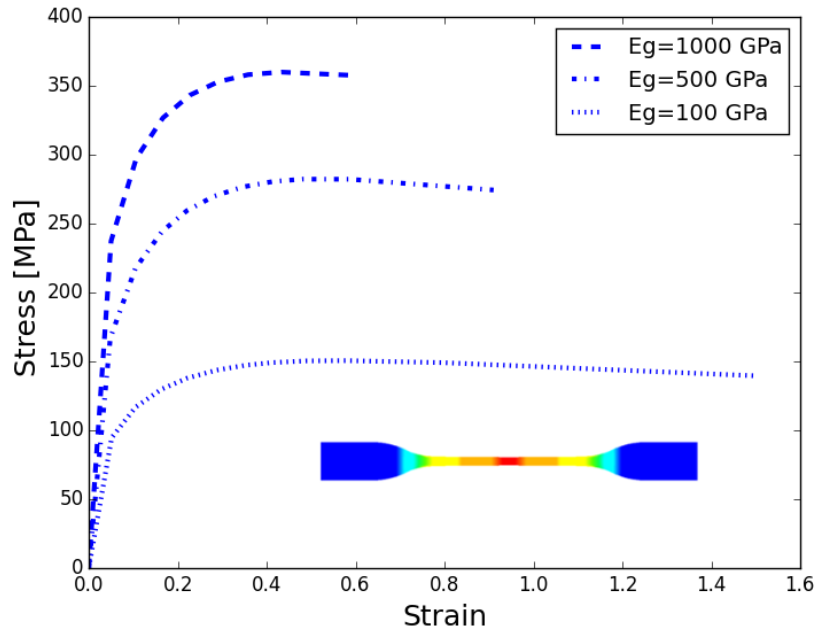
Figure 4. Normalised effective Young modulus versus GPL volume fraction

Figure 5. Effective Young modulus versus GPL aspect ratio AR

In Figure 6 is shown the nonlinear stress-strain response for a tensile specimen versus the GPL Young modulus E_g. An increase of the effective response with respect to high values of E_g. A determination of the maximal stress and strain is therefore carried out on these results for applications.
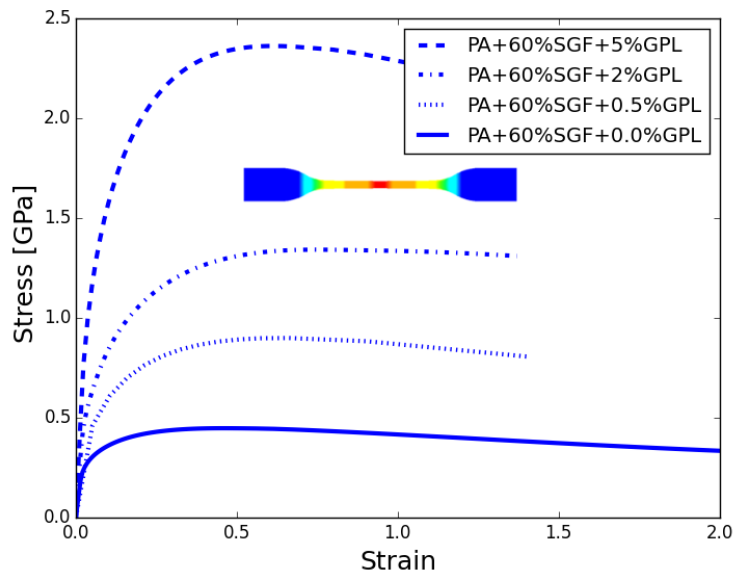
Figure 6. Stress-strain behaviour of the 2-phases composite under tensile test
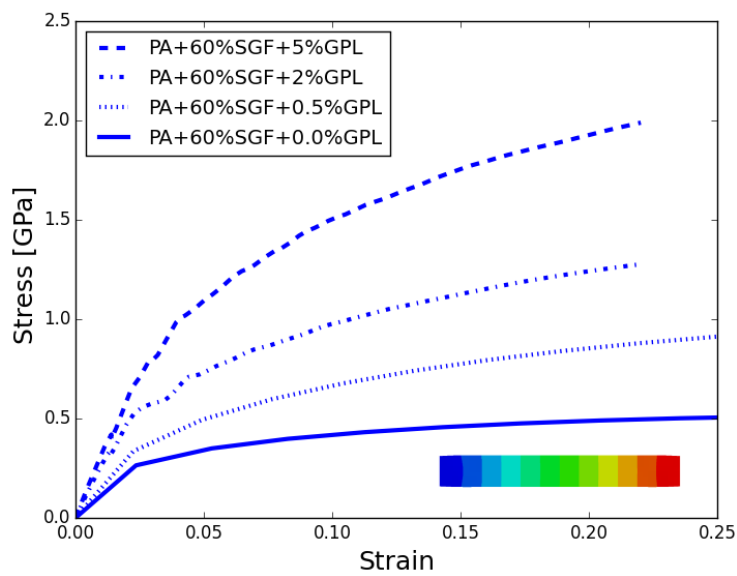
4.2. Three (3)-phases composite

E-short glass fibres are randomly embedded within a 3D random distribution of the 2-phases composite for the analysis of the 3-phases composite. Different volume fractions of GPL are considered mainly 0.5%, 2%, and 5%.

Figure 7(a) depicts the evolution of the effective stress-strain response of the 3-phases composite under tensile test. Results shift toward high stress with the increase of the GPL volume fraction. An increase in the composite stiffness in terms of Young modulus, initial yield strength and plastic hardening modulus are resulting from the volume fraction variation. The damage threshold is obtained when the softening point is reached for the determination of the ultimate tensile strength.
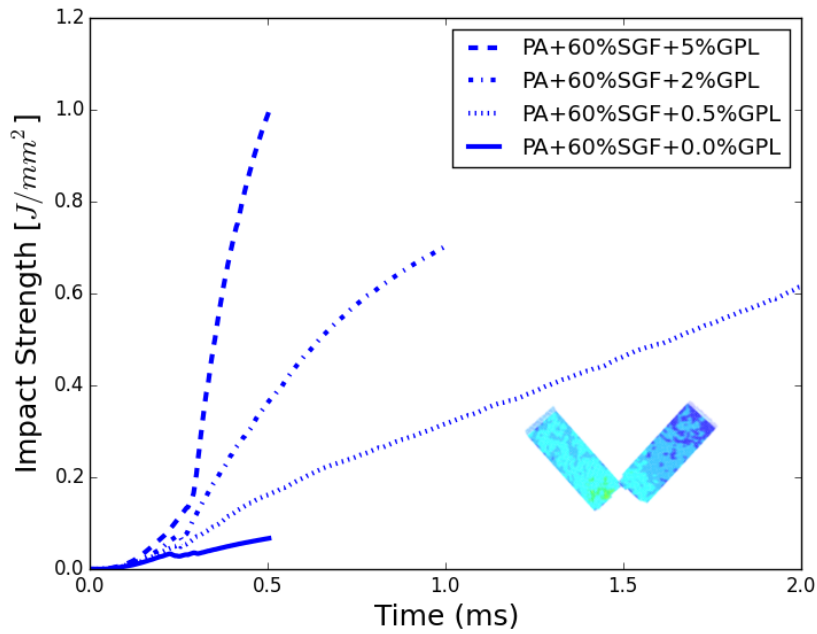
(a) Tensile

(b) Compression

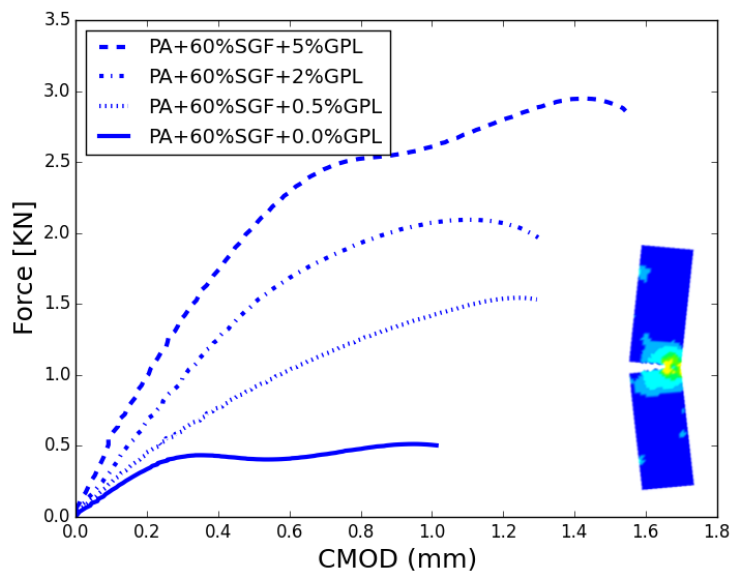**Figure 7.** Stress-strain behaviour of the 3-phases composite

For the compression, similar trends in term of Young modulus, initial yield strength and plastic hardening modulus are observed in Figure 7(b). However, the composite behaviour under the compression is different. The linear elastic stage is followed by the plastic zone where the composite yields and damages. Due to the densification resulting from material crushing together, no softening trend is observed leading to an increasing stiffer response. Both tests enable the characterisation of the damage/failure threshold for the ultimate tensile and compression strengths.

Besides, Figure 8 shows the impact strength of the 3-phases composite versus the applied load time. The impact strength characterises the capability to withstand by shock energy absorption from a
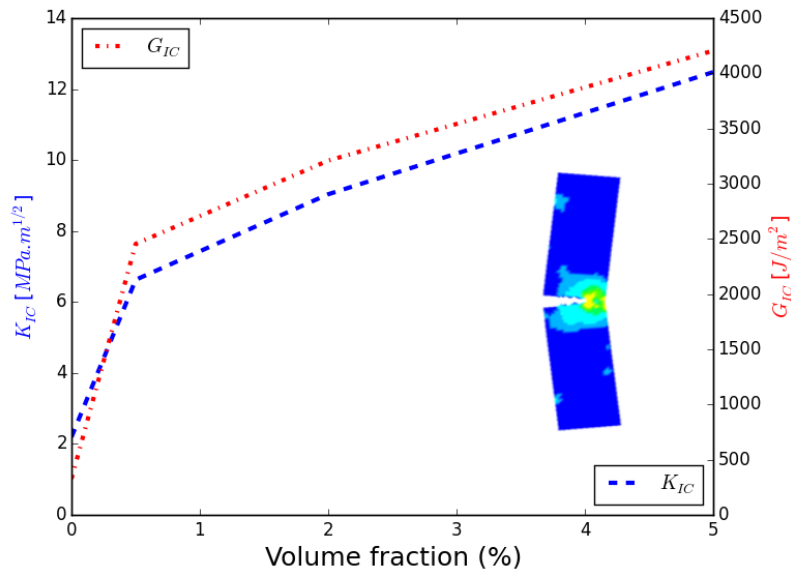
10

suddenly applied load. It shows higher values with the increase of the GPL volume fraction. Another interesting trend observed is related to the withstanding time. Indeed, the GPL volume fraction shows high impact strength for relatively low time. Therefore, GPL enhance the composite energy absorption capability in a short time period with a potential application for crashworthiness in automotive

Figure 8. Impact behaviour of the 3-phases composite
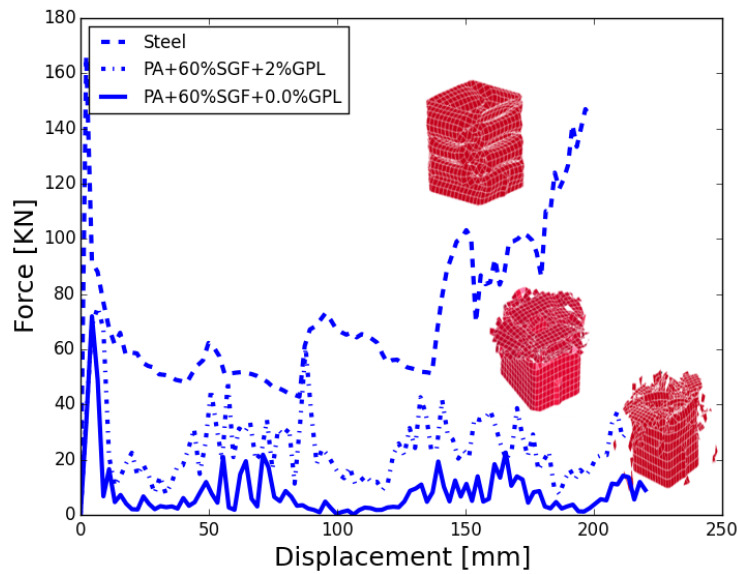

(a) Force versus CMOD

(b) Kic and Gic versus volume fraction

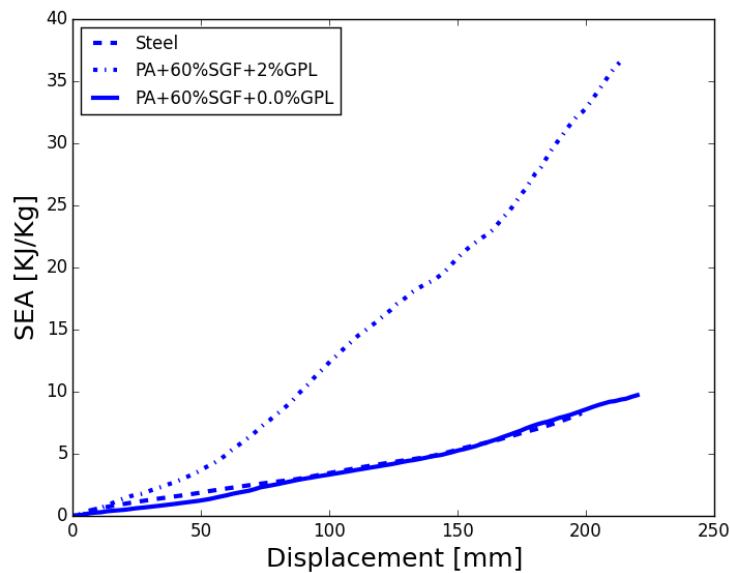**Figure 9.** Fracture toughness behaviour of the 3-phases composite

Furthermore, in Figure 9(a), the fracture toughness is analysed in terms of force versus crack mouth opening displacement CMOD. To reach the failure of the sample, results shift toward high force with the increase of the volume fraction. Moreover, these results enable the determination of the plane strain fracture toughness K_{IC} and the elastic strain energy rate G_{IC}. Figure 9(b) shows the evolution of K_{IC} and G_{IC} versus the GPL volume fraction. A nonlinear trend is noticed for both parameters while, the higher the volume fraction, the higher K_{IC} and G_{IC}.

4.3. Macroscale simulation of the crash box

Results from the 3-phases composite are implemented within LS-DYNA FE code as a user defined material subroutine (UMAT) from DIGIMAT-CAE. Figure 10 shows a full crash box simulation. The response of the 3-phases composite (2% graphene + 60% short fibres + 38% polymer PA) is compared with that of 2-phases composite (60% short fibres + 40% polymer PA) and the response provided by the steel.
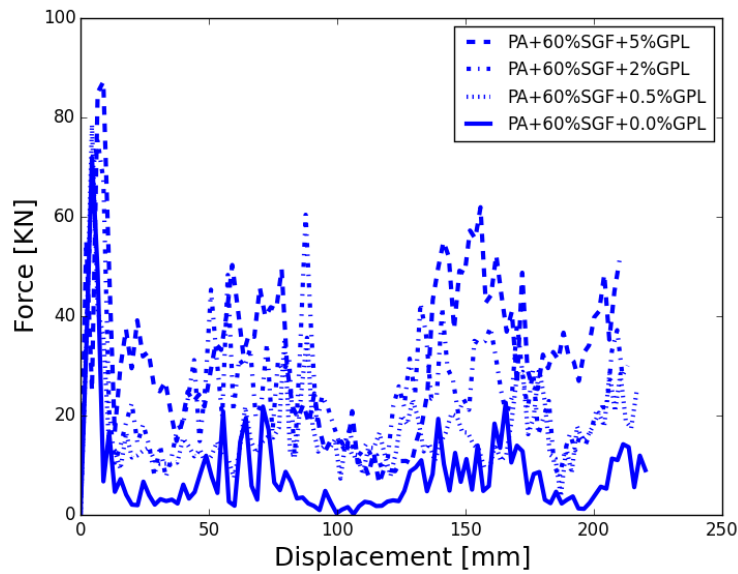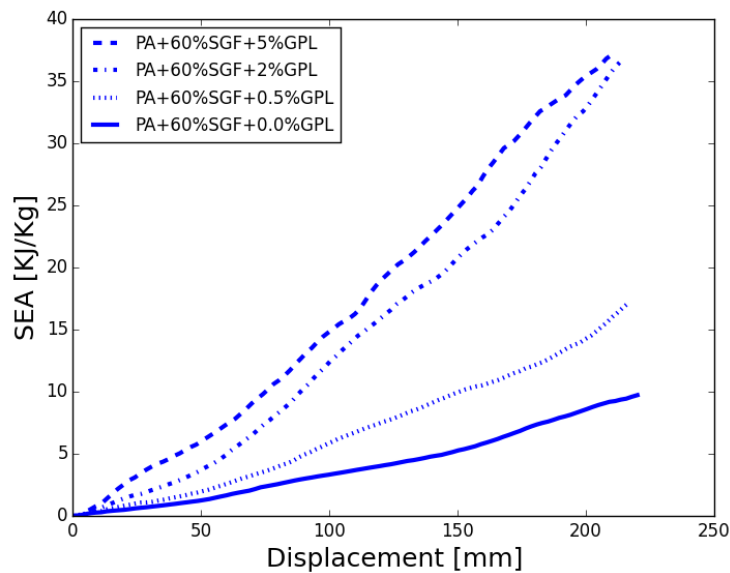
(a) Force versus displacement

(b) specific energy absorption versus displacement

Figure 10. Macroscale simulation for model comparison

The crush force-displacement curve of 2% GPL, is shown by Figure 10(a) along with the response obtained from a steel specimen as well as a polymer PA reinforced by short glass fibres without GPL. It can be seen that the peak crush force of both composite materials are two time lower compared to that is predicted by the steel while no significant difference is noticed between the composites peak force. However, the contribution of GPL is significant in terms of specific energy absorption SEA. That is illustrated by Figure 10(b) which displays the SEA for the three compared materials versus the displacement. While a slightly evolution is seen for the steel and the PA+60%SGF+0%GPL, the SEA shows a significant improvement with respect to the content of GPL in the PA+60%SGF+2%GPL.

(a) Force versus displacement

(b) specific energy absorption versus displacement

Figure 11. Volume fraction influence on the crashworthiness

Furthermore, from Figures 11(a)-(b), the crushing force-displacement and SEA are presented versus different GPL volume fraction. It is obtained from Figure 11(a) nearly a similar trend concerning the peak force for all range of volume fraction. Beyond the peak force domain, one can observe that the average force crush increases with the GPL volume fraction. In Figure 11(b), the evolution of the SEA is shown. The higher the GPL volume fraction, the higher the SEA showing the contribution of the GPL in the enhancement of the energy absorption.

5. Conclusion

The linkage between LS-Dyna FE code and Digimat homogenisation tools has been used to address the hierarchical multiscale crashworthiness modelling of the hybrid short-glass fibres reinforced graphene platelets polymer composite. The analysis consists on the modelling of the 2-phases graphene polymer composite whose effective properties are obtained from micromechanics formalism. Next, short glass fibres are embedded in the 2-phases composite to obtain the hybrid 3-phases composite. Numerical characterisation based on ASTM standard tests are performed in tensile and compression as well fracture toughness and Charpy impact.

The analysis of the 2-phases composite reveals an increase of effective Young modulus with the GPL volume fraction evolution. Low values of GPL aspect ratio AR have led to high effective Young modulus which starts decreasing when AR becomes larger. The 2D orientation configuration shows the most effective reinforcement character compared to the 3D orientation. The analysis of the hybrid 3-phases composite during a Charpy impact test shows that the impact strength remains sensitive to the GPL volume fraction. The higher the GPL volume fraction, the higher the impact strength. Furthermore, the fracture toughness indicates that the plane strain fracture toughness K_{IC} and the elastic strain energy rate G_{IC} shift toward high values when increasing the GPL volume fraction.

These results enable the determination of the damage and failure threshold for the simulation of a full structure under crashworthiness by considering different volume fraction of GPL. Results of the simulation indicate a reduction of the peak crush force when composite crush box is involved compared to the steel counterpart. While no significant variation in the reduction of the peak crush force is observed between neat composite i.e without GPL and composite with GPL, the volume fraction of GPL seems to significantly improve the specific energy absorption of the structure. As an outlook, this study needs to be extended to other derivatives of the graphene such as the graphene oxide GO [31] for examining the influence of a functionalisation of graphene in the full macro composite response. In addition, other properties (e.g. electrical conductivity behaviour [32]) to also be considered to maximise the impact of the modelling techniques developed in this paper on wider applications of science and engineering.

Acknowledgments

References

[1] A. Esnaola, I. Ulacia, L. Aretxabaleta, J. Aurrekoetxea, and I. Gallego. Quasi-static crush energy absorption capability of e-glass/polyester and hybrid e-glass basalt/polyester composite structures. *Materials & Design*, 76: 18 – 25, 2015. ISSN 0261-3069.

[2] Qiang Liu, Huanlin Xing, Yang Ju, Zhengyan Ou, and Qing Li. Quasi-static axial crushing and transverse bending of double hat shaped cfrp tubes. *Composite Structures*, 117: 1 – 11, 2014. ISSN 0263-8223.

[3] J. J. Carruthers, A. P. Kettle, and A. M. Robinson. Energy absorption capability and crashworthiness of composite material structures: A review. *Applied Mechanics Reviews*, 51 (10): 635–649, October 1998. ISSN 0003-6900.

[4] Abaqus and Dassault Systèmes. Simulation of the quasi-static crushing of a fabric composite plate. *Abaqus technology brief*, 2011.

[5] Tapas Kuilla, Sambhu Bhadra, Dahu Yao, Nam Hoon Kim, Saswata Bose, and Joong Hee Lee. Recent advances in graphene based polymer composites. *Progress in Polymer Science*, 35 (11): 1350 – 1375, 2010. ISSN 0079-6700.

[6] Robert J. Young, Ian A. Kinloch, Lei Gong, and Kostya S. Novoselov. The mechanics of graphene nanocomposites: A review. *Composites Science and Technology*, 72 (12): 1459 – 1476, 2012. ISSN 0266-3538.

[7] Sungjin Park and Rodney S. Ruoff. Chemical methods for the production of graphenes. *Nat Nano*, 4 (4): 217–224, April 2009. ISSN 1748-3387.

[8] Caterina Soldano, Ather Mahmood, and Erik Dujardin. Production, properties and potential of graphene. *Carbon*, 48 (8): 2127 – 2150, 2010. ISSN 0008-6223.

[9] M. Inagaki, Y. A. Kim, and M. Endo. Graphene: preparation and structural perfection. *J. Mater. Chem.*, 21: 3280–3294, 2011.

[10] Mohammed A. Rafiee, Javad Rafiee, Iti Srivastava, Zhou Wang, Huaihe Song, Zhong-Zhen Yu, and Nikhil Koratkar. Fracture and fatigue in graphene nanocomposites. *Small*, 6 (2): 179–183, 2010. ISSN 1613-6829.

[11] L. Monica Veca, Mohammed J. Meziani, Wei Wang, Xin Wang, Fushen Lu, Puyu Zhang, Yi Lin, Robert Fee, John W. Connell, and Ya-Ping Sun. Carbon nanosheets for polymeric nanocomposites with high thermal conductivity. *Advanced Materials*, 21 (20): 2088–2092, 2009. ISSN 1521-4095.

[12] Zhen Xu and Chao Gao. In situ polymerization approach to graphene-reinforced nylon-6 composites. *Macromolecules*, 43 (16): 6716–6723, 2010.

[13] Wen Ling Zhang, Bong Jun Park, and Hyoung Jin Choi. Colloidal graphene oxide/polyaniline nanocomposite and its electrorheology. *Chem. Commun.*, 46: 5596–5598, 2010.

[14] J. Cho, J.J. Luo, and I.M. Daniel. Mechanical characterization of graphite/epoxy nanocomposites by multi-scale analysis. *Composites Science and Technology*, 67 (1112): 2399 – 2407, 2007. ISSN 0266-3538.

[15] J.R. Xiao, B.A. Gama, and J.W. Gillespie Jr. An analytical molecular structural mechanics model for the mechanical properties of carbon nanotubes. *International Journal of Solids and Structures*, 42: 3075 – 3092, 2005. ISSN 0020-7683.

[16] Mahmood M. Shokrieh and Roham Rafiee. On the tensile behavior of an embedded carbon nanotube in polymer matrix with non-bonded interphase region. *Composite Structures*, 92 (3): 647 – 652, 2010. ISSN 0263-8223.

[17] Mahmood M. Shokrieh and Roham Rafiee. Investigation of nanotube length effect on the reinforcement efficiency in carbon nanotube based composites. *Composite Structures*, 92 (10): 2415 – 2420, 2010. ISSN 0263-8223.

[18] Mahmood M. Shokrieh and Roham Rafiee. Prediction of mechanical properties of an embedded carbon nanotube in polymer matrix based on developing an equivalent long fiber. *Mechanics Research Communications*, 37 (2): 235 – 240, 2010. ISSN 0093-6413.

[19] Mahmood M. Shokrieh and Roham Rafiee. Stochastic multi-scale modeling of cnt/polymer composites. *Computational Materials Science*, 50 (2): 437 – 446, 2010. ISSN 0927-0256.

[20] Y. Chandra, F. Scarpa, R. Chowdhury, S. Adhikari, and J. Sienz. Multiscale hybrid atomistic-fe approach for the nonlinear tensile behaviour of graphene nanocomposites. *Composites Part A: Applied Science and Manufacturing*, 46: 147 – 153, 2013. ISSN 1359-835X.

[21] Gaoming Dai and Leon Mishnaevsky Jr. Graphene reinforced nanocomposites: 3d simulation of damage and fracture. *Computational Materials Science*, 95: 684 – 692, 2014. ISSN 0927-0256.

[22] Bohayra Mortazavi, Olivier Benzerara, Hendrik Meyer, Julien Bardon, and Said Ahzi. Combined molecular dynamics-finite element multiscale modeling of thermal conduction in graphene epoxy nanocomposites. *Carbon*, 60: 356 – 365, 2013. ISSN 0008-6223.

[23] P. Vieville, A. S. Bonnet, and P. Lipinski. Modelling effective properties of composite materials using the inclusion concept. general considerations. *Arch. Mech.*, 58 (3): 207–239, 2006.

[24] I. Doghri and A. Ouaar. Homogenization of two-phase elasto-plastic composite materials and structures: Study of tangent operators, cyclic plasticity and numerical algorithms. *International Journal of Solids and Structures*, 40 (7): 1681 – 1712, 2003. ISSN 0020-7683.

[25] MSC Software Company. *Digimat User's Manual, E-xtream Engineering*, 2016.

[26] ASTM International. Standard test method for tensile properties of plastics d 638 - 02a.

[27] ASTM International. Standard test method for compressive properties of rigid plastics d 695.

[28] ASTM International. Standard test method for measurement of fracture toughness e 1820 – 01.

[29] ASTM International. Standard test methods for notched bar impact testing of metallic materials e23.

[30] Livermore Software Technology Corporation LSTC. *LS-DYNA, Keyword user's Manual*, 2014.

[31] R. Joshi, S. Alwarappanb, M. Yoshimurac, V. Sahajwallaa, and Y. Nishina. Graphene oxide: the new membrane material. *Appl.Mater. Today*, 1(1): 1–12, 2015.

[32] M. Ghislandi, E. Tkalya, A. Alekseev, C. Koning, G. de With. Electrical conductive behavior of polymer composites prepared with aqueous graphene dispersions, *Appl.Mater. Today*, 1(2): 88-94, 2015

Highlights:

- The overall properties of 2-phases graphene platelets GPL/polymer are determined using a mean-field based homogenisation technique;
- The hybrid 3-phases composite consists on a hierarchical double-scale approach combining the 2-phases GPL/polymer composite with short glass fibres;
- A crashworthiness test is simulated by implementing the constitutive laws of the 3-phases glass fibres/graphene polymer composite using the linkage Digimat-CAE/LS-Dyna;
- A decrease of the crush force peak is noticed for the 3-phases composite;
- The specific energy absorption SEA of the 3-phases composite is improved compared to conventional steel and composites.